

# 600 km repeater-like quantum communications with dual-band stabilisation

Mirko Pittaluga<sup>1,2†\*</sup>, Mariella Minder<sup>1,3†</sup>, Marco Lucamarini<sup>1\*</sup>, Mirko Sanzaro<sup>1</sup>,

Robert I. Woodward<sup>1</sup>, Ming-Jun Li<sup>4</sup>, Zhiliang Yuan<sup>1</sup> & Andrew J. Shields<sup>1</sup>

<sup>1</sup>*Toshiba Europe Limited, 208 Cambridge Science Park,  
Cambridge CB4 0GZ, UK*

<sup>2</sup>*School of Electronic and Electrical Engineering,  
University of Leeds, Leeds LS2 9JT, UK*

<sup>3</sup>*Department of Engineering, Cambridge University,  
9JJ Thomson Avenue, Cambridge CB3 0FA, UK*

<sup>4</sup>*Corning Incorporated, Corning, New York, 14831, USA*

<sup>†</sup>*These authors contributed equally to this work*

\*[mirko.pittaluga@crl.toshiba.co.uk](mailto:mirko.pittaluga@crl.toshiba.co.uk)

\*[marco.lucamarini@crl.toshiba.co.uk](mailto:marco.lucamarini@crl.toshiba.co.uk)

(ΩDated: Thursday 25<sup>th</sup> June, 2020)

Twin-field (TF) quantum key distribution (QKD) could fundamentally alter the rate-distance relationship of QKD, offering the scaling of a single-node quantum repeater. Although recent experiments have demonstrated the potential of TF-QKD, formidable challenges remain for its real world use. In particular, new methods are needed to extend both the distance beyond 500 km and key rates above current milli-bit per second values. Previous demonstrations have required intense stabilisation signals at the same wavelength as the quantum channel, thereby unavoidably generating noise due to Rayleigh scattering that limits the distance and bit rate. Here, we introduce a novel dual band stabilisation scheme based on wavelength division multiplexing that allows us to circumvent past limitations. An intense stabilisation signal that is spectrally isolated from the quantum channel is used to reduce the phase drift by three orders of magnitude, while a second, much weaker reference at the quantum wavelength locks the channel phase to a predetermined value. With this strategy, we realise a low noise implementation suitable for all the variants of TF-QKD protocols proposed so far and capable of generating real strings of bits for the first time. The setup provides repeater-like key rates over record communication distances of 555 km and 605 km in the finite-size and asymptotic regimes, respectively, and increases the secure key rate at long distance by two orders of magnitude to values of practical significance.

## INTRODUCTION

Quantum key distribution (QKD) [1, 2] allows two distant users to establish a common secret string of bits by sending photons through a communication line, often an optical fibre. The photons, however, are scattered by the propagation medium and have only a small probability of reaching the end of the line, which restrains the QKD key rate and transmission range. A rigorous theorem [3] (see also [4]) limits to  $1.44\eta$  the number of secure bits delivered by QKD over a line with small transmission probability  $\eta$ , a limit known as ‘repeaterless secret key capacity’ [3] ( $\text{SKC}_0$ ). Quantum repeaters offer a theoretical solution to extend the range of QKD [5–8]. However, a full-fledged quantum repeater remains outside the reach of present technology, due to the difficulty in building and reliably operating a low-loss quantum memory. A partial implementation of a memory-assisted repeater has been recently achieved [9] in the form of measurement-device-independent QKD [10] (see also [11]).

An alternative method to extend the transmission range of QKD without using a quantum memory has been recently discovered and named ‘twin-field’ (TF) QKD [12] due to the peculiar interference between two fields that have similar, though not identical, optical phase. The secret key rate (SKR) of TF-QKD scales pro-

portionally to  $\sqrt{\eta}$ , similar to a quantum repeater with a single node, thus entailing a major increase in the SKR-vs-distance figure of QKD. This has led to the realisation of several experiments that display formidable long-range (or high-loss) characteristics [13–18].

The security of the original TF-QKD protocol was first proved in [12] for a limited class of attacks and then extended to general attacks in [19] and [20]. Soon after, its experimental implementation was also considerably simplified thanks to protocol variants that waived the need for phase randomisation and reconciliation for signal states [21–26]. The ‘phase-matching’ protocols [21–23] feature signal states with a constant global phase while the ‘sending’ or ‘not-sending’ protocol (SNS) [24–26] encode qubits upon optical pulses with random and unknown phases. With the help of ‘two-way classical communication’ (TWCC) [27], the SNS protocol is able to remove the quantum bit error rate (QBER) floor intrinsic to the encoding method thereby extending the communication distance. By running the TWCC protocol over ultralow-loss (ULL) optical fibres, a distance of 509 km has been achieved [18], which represents the current record distance for secure quantum communications over optical fibres.

In order to perform TF-QKD, it is necessary to compensate the phase drift of the quantum pulses interfer-

ing in the intermediate node (Charlie) after travelling through hundreds of kilometres in fibre. The typical phase drift for a 100 km fibre was measured to exceed 1000 rad/s [12]. Compensation of rapid drift requires bright reference light to be transmitted in the same fibre along with the quantum signals for phase calibration. The longer the fibre, the brighter the reference pulses have to be, as phase calibration requires a minimum power level to be received at the detectors. So far, all the TF-QKD experiments used the same wavelength for both quantum and reference signals, with the help of time-divisional modulation to achieve the necessary intensity contrast. However, this approach ceases to work for ultralong fibres. The ever-increasing intensity of the reference pulses causes a strong Rayleigh scattering that travels back and forth along the fibre and dramatically reduces the quantum signal to noise ratio. As it was proven in [18], the noise due to double Rayleigh scattering becomes comparable with the dark counts noise of Charlie's detectors around 500 km of ultralow-loss fibre. Moreover, the performance of a system using a single wavelength for both dim and bright signals will be inevitably limited by the finite dynamic range of the detectors. These two aspects fundamentally limit 'single-band' TF-QKD.

In this work, we adopt a novel 'dual band' phase control using two wavelengths multiplexed on a single fibre. It allows strong intensity contrast between reference and quantum signals while the wavelength separation prevents the Rayleigh scattering from contaminating the quantum signals. An active phase compensation of the intense reference light leads to an immediate reduction of the phase drift by more than a factor 1000, allowing the residual drift to be compensated at a much slower pace using light signals that have comparable intensity and identical wavelength as the quantum signals. It is worth noticing that the two wavelengths are generated by independent lasers and are not phase-locked, i.e., the stabilisation mechanism works also without an exact phase relation between the two bands. This counter-intuitive detail is fundamental to guarantee the practicality of the setup, which makes ultra-stable cavities or complex light modulation schemes unnecessary.

The resulting setup is versatile, capable of implementing all kinds of TF-QKD protocols proposed so far, including the phase-matching ones [21–23], which cannot be efficiently run without an active phase stabilisation method. With this setup, clocked at 1 GHz, we run various protocols and achieve record SKRs and distances for secure quantum communications over optical fibres. The SKR overcomes the absolute SKC<sub>0</sub> at several distances, thus proving the quantum repeater-like behaviour of our system. In addition to estimating the SKR, we also extract, for the first time, actual raw bits from a TF-QKD protocol. This is a necessary requisite for a system that aims to distribute secure cryptographic keys to remote users in a real-world scenario.

## EXPERIMENTAL SETUP

The experimental setup (Fig. 1) is composed of three modules. The modules of Alice and Bob, who are the communicating users, are connected to Charlie's module via the quantum channel, made of spools of Corning SMF-28 ULL fibre. The spools are spliced into different sets, thus enabling experiments over 5 different communication distances, ranging from 153.2 to 605.2 km. The average loss coefficient of the fibre channel, including splices and connectors, is 0.171 dB/km. For detailed information on the fibre properties, refer to the Supplementary Material.

The setup uses lasers L<sub>1</sub> and L<sub>2</sub> emitting at  $\lambda_1$  (1550.12 nm) and  $\lambda_2$  (1548.51 nm), respectively. Each user owns a narrow bandwidth ( $\Delta\nu = 50$  kHz) continuous-wave (CW) L<sub>1</sub> laser, which is locked to the other user's L<sub>1</sub> via an optical phase locked loop (OPLL) and a service fibre [13]. The encoders operate at 1 GHz, and they carve the  $\lambda_1$  input light into a train of 250 ps pulses. The even-numbered pulses are further modulated in intensity and phase, according to the requirements of the different TF-QKD protocols to be implemented. We refer to these as 'quantum signals'. The odd-numbered pulses do not receive any further modulation and are used to track the phase drift of the quantum signals. Hence, we refer to them as 'dim reference'. All pulses are attenuated to the single-photon level before entering the quantum channel. A step-by-step description of the encoder modulation is given in the Methods. For fast phase tracking, the laser L<sub>2</sub> provides a 'bright reference' at wavelength  $\lambda_2$  for the whole system. Through dense-wavelength-division multiplexing (DWDM), the bright reference shares the same service and quantum fibres as the dim reference and the quantum signals. This is an important requirement for effective phase stabilisation, together with the condition that  $\lambda_2$  generates interference in Charlie's module. We found that this condition can be easily satisfied by our L<sub>2</sub> laser which features a bandwidth  $\Delta\nu = 150$  kHz.

Alice and Bob provide independent pre-compensation of the polarisation rotation of the signals at the two wavelengths so that all photons arrive with identical polarisation at Charlie's 50/50 beam-splitter. The interference output at the beam-splitter are separated by DWDM filters before detection by three superconducting nanowire single photon detectors (SNSPD's): D<sub>0</sub> and D<sub>1</sub> for  $\lambda_1$  photons and D<sub>2</sub> for  $\lambda_2$  photons. Charlie's module further contains a phase modulator (PM) in one input arm and a fibre stretcher (FS) sandwiched between a pair of DWDMs in the other arm. Full stabilisation of the quantum signal is achieved in two steps, each step using a specific wavelength of the dual-band stabilisation. First, Charlie measures the bright reference and uses a field programmable gate array (FPGA) with an integrated counter to apply a proportional-integral-differential (PID) control to the bias of his PM. The brightness of the signal detected by D<sub>2</sub> allows this con-

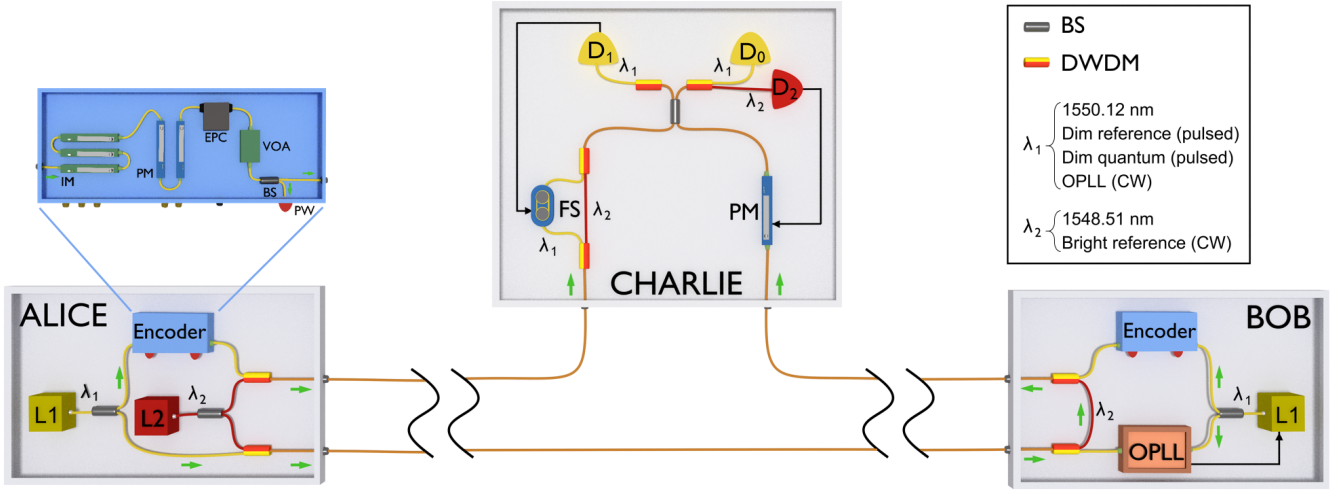


**FIG. 1. Experimental setup.** Alice and Bob generate  $\lambda_1$  (yellow fibres in the schematic) using local CW lasers  $L_1$ . A set of intensity and phase modulators inside each user’s Encoder allow them to run different TF-QKD protocols. A second laser ( $L_2$ ) generates the bright reference signal  $\lambda_2$  (red fibres) used for fast phase stabilisation. A service fibre (lower one in the figure) distributes the  $\lambda_1$  and  $\lambda_2$  wavelengths. After locking the  $L_1$  lasers through an OPLL, the users multiplex the wavelengths in the quantum channel (upper fibres in the figure) and send them to Charlie. At Charlie, a beam splitter (BS) combines Alice’s and Bob’s signals, while the dual band phase stabilisation realised by a phase modulator (PM) and a fibre stretcher (FS) removes the phase noise introduced by the quantum channel. SNSPDs  $D_0$  and  $D_1$  record the interference output for  $\lambda_1$ , while  $D_2$  records the one for  $\lambda_2$ . **Encoder boxes.** IM: intensity modulator, PM: phase modulator, EPC: electrical polarisation controller, VOA: Variable optical attenuator, BS: Beam splitter.

trol loop to operate at 200 kHz, sufficient to stabilise the phase drift caused by the long fibre channels. Since  $\lambda_1$  and  $\lambda_2$  share the same fibre and are spectrally close, the light at  $\lambda_2$  can be used to stabilise the phase of the pulses at  $\lambda_1$ . Assuming unidirectional phase drift, the  $\lambda_2$ -stabilisation will reduce the phase drift in  $\lambda_1$  by approximately  $\lambda_1/|\lambda_2 - \lambda_1| \approx 1000$ . In the real scenario, the non-unidirectionality of the phase drift makes the actual reduction even greater, as we will show later. The slowed drift can then be comfortably corrected through a second PID controller adjusting the bias of the FS at a rate of 10-20 Hz, without requiring an intense input signal. The input signal for this feedback is provided by the interference outcome of the dim reference pulses at  $\lambda_1$  recorded by  $D_1$ . More information about the feedback systems is provided in the Supplementary Materials.

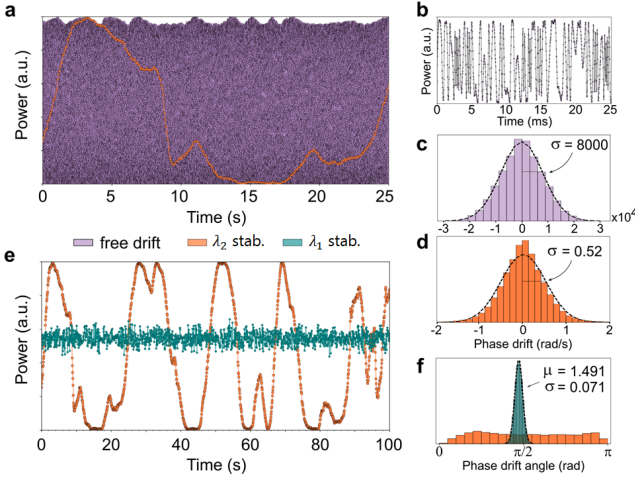
## RESULTS

Fig. 2 shows the interference outcome for  $\lambda_1$ , over a 555 km long quantum channel, at different stages of the stabilisation process. The purple dots in Fig. 2a represent the interference when no phase stabilisation is applied. At this distance, the free drift is so rapid (in the order of  $10^4$  rad/s) that it is impossible to discern any interference fringe over a 1 s time scale. Only on a millisecond time scale (see Fig. 2b) can we distinguish the interference fringes. The phase drift rate distribution associated with this measurement is shown in the purple histogram in

Fig. 2c. Its standard deviation allows us to quantify the phase drift in  $8 \cdot 10^3$  rad/s.

After activating the stabilisation from  $\lambda_2$ , the phase drift rate for  $\lambda_1$  reduces drastically (see orange points in Fig. 2a). It is now possible to follow the evolution of constructive or destructive interference over a time scale of tens of seconds. The effectiveness of this stabilisation is quantifiable by the reduction in the phase drift rate for the recorded data (orange histogram in Fig. 2d). When feedback from the bright reference at  $\lambda_2$  is enabled, the standard deviation of the drift rate decreases to 0.52 rad/s, a value 16000 times smaller than without the bright reference stabilisation. This reduction is considerably better than the estimated factor 1000 due to the cancellation of rapid opposite drifts. After  $\lambda_2$  stabilisation, a residual slow phase drift is still present for  $\lambda_1$ . This can be readily compensated by using the dim reference pulses at  $\lambda_1$ , which leads to a stable interference output (teal dots in Fig. 2e) that can be centered around any arbitrary value. Fig. 2f shows the phase distribution between the interfering  $\lambda_1$  signals locked to have  $\pi/2$  difference. The locking error is only 0.071 rad (standard deviation of the teal coloured distribution in the figure), which contributes to the QBER by less than 2%.

Using the described dual band stabilisation, we performed four experiments with different TF-QKD protocols, varying the operational regimes and optimising the parameters in each case. Firstly, the CAL [22] and SNS [24] protocols in the asymptotic regime, then the SNS with the TWCC method [27], both in the asymp-



**FIG. 2. Dual band stabilisation.** All the data in this figure has been recorded at 555 km of optical fibre with a power meter for easier comparison. The colour code is purple for free drift, teal for  $\lambda_1$ -stabilised and orange for  $\lambda_2$ -stabilised data. **a**, Comparison between free drifting and  $\lambda_2$ -stabilised data. Acquisition times were 25  $\mu$ s and 60 ms for free drifting and  $\lambda_2$ -stabilised data, respectively, due to the different time scales. **b**, Same data set as in (a) but over a ms time scale. **c**, Histogram of the free drifting phase drift. The standard deviation is 8000 rad/s. **d**, Histogram of the  $\lambda_2$ -stabilised phase drift. The standard deviation is 0.52 rad/s, i.e. about 16000 times smaller than in sub-figure (d). **e**, Comparison between  $\lambda_2$ -stabilised data (orange) and data stabilised using both wavelengths,  $\lambda_1$  and  $\lambda_2$  (teal). **f**, Phase offset distributions for the data shown in (e).  $\lambda_2$ -stabilised data has an almost uniform distribution over  $[0, \pi]$  whereas  $\lambda_1$ -stabilised data has a distribution peaked around  $\pi/2$ .

totic and in the finite-size regimes [25, 26]. In the practically relevant case of finite-size TWCC-SNS, we also extracted real bits of the raw key. Details about the protocol parameters, together with additional information on the patterns used for encoding, are given in the Supplementary Material.

In Fig. 3 we report our results in terms of SKR versus distance, together with the simulation curves and the state-of-the-art SKRs for long-distance TF-QKD [17, 18] and QKD [28] over optical fibres. In the same graph we also plot the absolute  $\text{SKC}_0$ , which assumes ideal equipment for Alice and Bob and hence is the most difficult bound to overcome. Surpassing this limit proves the repeater-like behaviour of our setup. The complete experimental results can be found in the Supplementary Materials. The CAL and SNS protocols have been implemented on a 368.7 km-long optical fibre (62.8 dB loss) and analysed in the asymptotic scenario. For CAL, we obtain an SKR of 852.7 bit/s, 2.39 times larger than  $\text{SKC}_0$ . For SNS, the SKR is 549.2 bit/s, 1.54 times larger than  $\text{SKC}_0$ . In order to reach longer distances, we resort to TWCC-SNS. We take measurements at 153.3, 368.7, 522.0, 555.2 and 605.2 km, i.e., from 26.5 dB to 104.8 dB loss, and we extract positive SKRs both in the asymptotic

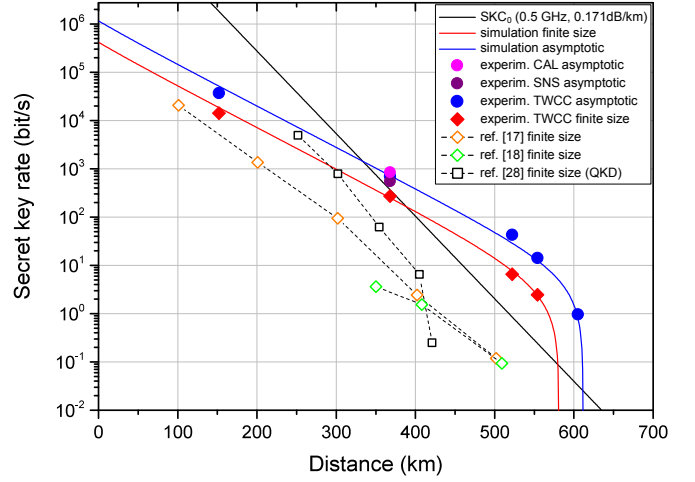


**FIG. 3. Key rate simulations and results.** Secret key rates are plotted against the quantum channel length. This is constituted by ultra-low loss (ULL) fibres of 0.171 dB/km loss. The  $\text{SKC}_0$  bound for unitary detection efficiency (black line) is plotted along the simulations for the TWCC SNS TF-QKD protocol in the asymptotic and finite size regimes (blue and red curves respectively). Filled markers show the experimental results we obtained for the different protocols whereas unfilled markers are the state of the art results in term of SKR over distance for fibre-based TF-QKD [17, 18] (diamonds) and QKD [28] (squares).

totic and in the finite-size regimes (blue and red points in Fig. 3, respectively). At 555 km, with only 2 hours of continuous measurement, we are able to extract a finite-size SKR of 2.468 bit/s, a value 10 times higher than the absolute  $\text{SKC}_0$ . At 605.2 km, with a loss budget of 104.8 dB, we achieve an asymptotic SKR of 0.969 bit/s, which is 30 times higher than the  $\text{SKC}_0$ . This represents the first fibre-based secure quantum communication beyond the barriers of 600 km and 100 dB.

To further appreciate the progress entailed by our new technique, we compare our results with the experimental points setting the current record distances for fibre-based QKD (421 km [28]) and TF-QKD (502 km [17], 509 km [18]). Distance-wise, there is an increase of tens of (more than a hundred) kilometres over TF-QKD (QKD) prior art. Rate-wise the advancement is even more pronounced, with 2 orders of magnitude improvement over the SKR of the furthest point achieved so far.

All the TF-QKD experiments performed so far, as well as the vast majority of long-distance QKD experiments, have only provided an in-principle estimation of the SKR without a real extraction of the bits that form a cryptographic key after suitable post-processing. In our experiment, we extract real strings of bits from the SNS protocol and process them with the TWCC method. The generation of raw bits is a challenging task, especially with a clock rate as high as 1 GHz, as it requires individual tagging and real-time manipulation of the signals recorded at the detectors. Fig. 4 gives a graphical representation of the TWCC method applied to a raw bit string extracted

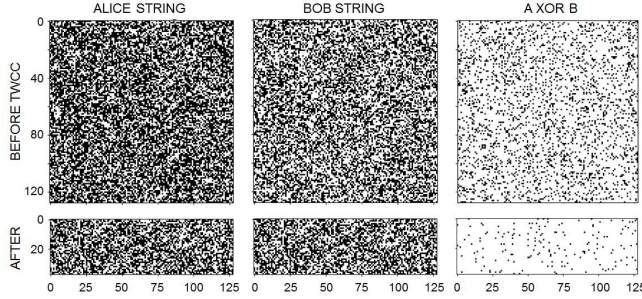


**FIG. 4. Binary maps of the extracted bit strings.** Samples of the bits extracted from the experiment performed at 522 km before (top panels) and after (bottom panels) TWCC is applied. *Top* - The first two squares on the left ( $128 \times 128$  pixels) are a sample of the users' raw strings before TWCC is applied, with white (black) pixels associated with the bit value 0 (1). The third square on the right is obtained by modulo-2 addition (XOR) of the first two. The black dots in this square represent the errors in the strings. *Bottom* - Refined keys after TWCC has been applied. The strings shrink by 70% into rectangles with  $128 \times 38$  pixels. Reduction in key size is accompanied by a substantial reduction in the key errors, as is apparent from the rightmost rectangle.

during the experiment performed at 522 km. The bits of the strings are displayed as white or black pixels depending on their value 0 or 1, respectively. The leftmost and central panels in the first row show Alice's and Bob's raw strings, distilled from the SNS protocol, whereas the rightmost panel reports the bitwise addition of the two strings. The density of the dots in the first two panels reveal a slight bias (53.8%) in the bit value which is intrinsic to the SNS protocol [24]. A simulation shows that with our parameters a bias of 52.7% has to be expected. On the other hand, the black dots in the rightmost panel highlight the conflicting bits in the users' raw keys, which amount to a 16% of the total. The second row of Fig. 4 shows the effect of TWCC on the users strings. TWCC induces a considerable reduction of the errors, from 16% to 3.5%, and of the bias in the strings at the expenses of the strings length, which decreases by  $\sim 70\%$ . However, the overall effect of TWCC is beneficial, as it increases the signal-to-noise ratio of the raw keys and so also the range of TF-QKD.

## CONCLUSIONS

We have shown that dual band phase stabilisation can dramatically reduce the phase fluctuations on optical fibre by more than four orders of magnitude. This has allowed us to overcome the fundamental noise limitation of long distance TF-QKD and increase its secret key rate from the current millibit per second range to the bit per second range for the longest fibre length. Our setup tolerates a maximum loss beyond 100 dB allowing quantum communication over 600 km of fibre for the first time. We believe these techniques will have more general application in quantum communications, for example enabling DLCZ-type quantum repeaters [6], quantum fingerprint [29–31] over longer distances or a phase-based architecture for the quantum internet [32].

## ACKNOWLEDGMENTS

We thank Xiang-Bin Wang and Hai Xu for their useful feedback on the TWCC protocol. The authors acknowledge funding from the European Union's Horizon 2020 research and innovation programme under the grant agreement No 857156 "OPENQKD" and under the Marie Skłodowska-Curie grant agreement No 675662. M.M. acknowledges financial support from the Engineering and Physical Sciences Research Council (EPSRC) and Toshiba Europe Ltd.

**Author contributions.** M.P. and M.M. developed the experimental set-up, performed the measurements and analysed the data. M.S. and R.I.W. supported the experimental work. M.-J.L. provided the ultralow-loss fibres. Z.L.Y., M.L. and A.J.S. guided the work. M.L., M.P. and M.M. provided the simulations and wrote the manuscript, with contributions from all the authors.

**Competing interests.** The authors declare no competing interests.

**Data availability.** The data that support the plots within this paper and other findings of this study are available from the corresponding authors on reasonable request.

**Correspondence and requests for materials.** should be addressed to M.L. and M.P.

---

- [1] Bennett, C. H. & Brassard, G. Quantum cryptography: Public key distribution and coin tossing. *Theor. Comput. Sci.* **560**, 7–11 (2014).
- [2] Ekert, A. K. Quantum cryptography based on Bell's theorem. *Phys. Rev. Lett.* **67**, 661–663 (1991).
- [3] Pirandola, S., Laurenza, R., Ottaviani, C. & Banchi, L. Fundamental limits of repeaterless quantum communications. *Nat. Commun.* **8**, 15043 (2017).
- [4] Takeoka, M., Guha, S. & Wilde, M. M. Fundamental rate-loss tradeoff for optical quantum key distribution. *Nat. Commun.* **5**, 5235 (2014).
- [5] Briegel, H.-J., Dür, W., Cirac, J. I. & Zoller, P. Quantum repeaters: The role of imperfect local operations in quantum communication. *Phys. Rev. Lett.* **81**, 5932–5935 (1998).
- [6] Duan, L.-M., Lukin, M. D., Cirac, J. I. & Zoller, P. Long-

distance quantum communication with atomic ensembles and linear optics. *Nature* **414**, 413–418 (2001).

[7] Sangouard, N., Simon, C., de Riedmatten, H. & Gisin, N. Quantum repeaters based on atomic ensembles and linear optics. *Rev. Mod. Phys.* **83**, 33–80 (2011).

[8] Guha, S. *et al.* Rate-loss analysis of an efficient quantum repeater architecture. *Phys. Rev. A* **92**, 022357 (2015).

[9] Bhaskar, M. K. *et al.* Experimental demonstration of memory-enhanced quantum communication. *Nature* **580**, 60–64 (2020).

[10] Lo, H.-K., Curty, M. & Qi, B. Measurement-device-independent quantum key distribution. *Phys. Rev. Lett.* **108**, 130503 (2012).

[11] Braunstein, S. L. & Pirandola, S. Side-channel-free quantum key distribution. *Phys. Rev. Lett.* **108**, 130502 (2012).

[12] Lucamarini, M., Yuan, Z. L., Dynes, J. F. & Shields, A. J. Overcoming the rate-distance limit of quantum key distribution without quantum repeaters. *Nature* **557**, 400–403 (2018).

[13] Minder, M. *et al.* Experimental quantum key distribution beyond the repeaterless secret key capacity. *Nat. Photonics* **13**, 334–338 (2019).

[14] Wang, S. *et al.* Beating the fundamental rate-distance limit in a proof-of-principle quantum key distribution system. *Phys. Rev. X* **9**, 021046 (2019).

[15] Liu, Y. *et al.* Experimental twin-field quantum key distribution through sending or not sending. *Phys. Rev. Lett.* **123**, 100505 (2019).

[16] Zhong, X., Hu, J., Curty, M., Qian, L. & Lo, H.-K. Proof-of-principle experimental demonstration of twin-field type quantum key distribution. *Phys. Rev. Lett.* **123**, 100506 (2019).

[17] Fang, X.-T. *et al.* Implementation of quantum key distribution surpassing the linear rate-transmittance bound. *Nature Photonics* (2020).

[18] Chen, J.-P. *et al.* Sending-or-not-sending with independent lasers: Secure twin-field quantum key distribution over 509 km. *Phys. Rev. Lett.* **124**, 070501 (2020).

[19] Tamaki, K., Lo, H.-K., Wang, W. & Lucamarini, M. Information theoretic security of quantum key distribution overcoming the repeaterless secret key capacity bound. *arXiv:1805.05511* (2018). arXiv:1805.05511.

[20] Ma, X., Zeng, P. & Zhou, H. Phase-matching quantum key distribution. *Phys. Rev. X* **8**, 031043 (2018). arXiv:1805.05538.

[21] Lin, J. & Lütkenhaus, N. Simple security analysis of phase-matching measurement-device-independent quantum key distribution. *Phys. Rev. A* **98**, 042332 (2018).

[22] Curty, M., Azuma, K. & Lo, H.-K. Simple security proof of twin-field type quantum key distribution protocol. *npj Quantum Information* **5**, 64 (2019).

[23] Cui, C. *et al.* Twin-field quantum key distribution without phase postselection. *Phys. Rev. Applied* **11**, 034053 (2019). arXiv:1807.02334.

[24] Wang, X.-B., Yu, Z.-W. & Hu, X.-L. Twin-field quantum key distribution with large misalignment error. *Phys. Rev. A* **98**, 062323 (2018). arXiv:1805.09222.

[25] Jiang, C., Yu, Z.-W., Hu, X.-L. & Wang, X.-B. Unconditional security of sending or not sending twin-field quantum key distribution with finite pulses. *Phys. Rev. Applied* **12**, 024061 (2019).

[26] Yu, Z.-W., Hu, X.-L., Jiang, C., Xu, H. & Wang, X.-B. Sending-or-not-sending twin-field quantum key distribution in practice. *Sci. Rep.* **9**, 3080 (2019). arXiv:1807.09891.

[27] Xu, H., Yu, Z.-W., Jiang, C., Hu, X.-L. & Wang, X.-B. Sending-or-not-sending twin-field quantum key distribution: Breaking the direct transmission key rate. *Phys. Rev. A* **101**, 042330 (2020).

[28] Boaron, A. *et al.* Secure quantum key distribution over 421 km of optical fiber. *Phys. Rev. Lett.* **121**, 190502 (2018). arXiv:1807.03222.

[29] Arrazola, J. M. & Lütkenhaus, N. Quantum fingerprinting with coherent states and a constant mean number of photons. *Phys. Rev. A* **89**, 062305 (2014).

[30] Xu, F. *et al.* Experimental quantum fingerprinting with weak coherent pulses. *Nat. Commun.* **6**, 8735 (2015).

[31] Zhong, X., Xu, F., Lo, H.-K. & Qian, L. Efficient experimental quantum fingerprinting with wavelength division multiplexing. *arXiv:2005.06049* (2020). 2005.06049v1.

[32] Kimble, H. J. The quantum internet. *Nature* **453**, 1023–1030 (2008).

[33] Wang, X.-B. Beating the photon-number-splitting attack in practical quantum cryptography. *Phys. Rev. Lett.* **94**, 230503 (2005).

[34] Lo, H.-K., Ma, X. & Chen, K. Decoy state quantum key distribution. *Phys. Rev. Lett.* **94**, 230504 (2005).

## METHODS

**Encoder boxes.** For a detailed representation of the components inside the encoder boxes see inset diagram in Fig. 1. The incoming CW light arrives already aligned in polarisation with the optical axes of the subsequent modulators. The first components in the encoders are three intensity modulators (IMs), used to carve 250 ps long pulses at a 1 GHz rate, with three possible intensity levels ( $u, v, w$ ). The intensity ratios between the different intensity levels can be adjusted by the AC amplitude driving the IMs.

Two phase modulators (PMs) are then used to encode the phase of the optical pulses. In this system, we cascade two PMs instead of using just one to reduce their RF signal amplitudes. Limiting each PM to have a modulation range of  $[-\pi/2, \pi/2]$ , we achieve a phase modulation that covers the whole  $[0, 2\pi]$  range and that is linear with its driving signal amplitude. Each PM is driven by a 8-bit DACs, and with two cascaded we are able to encode 512 different phase values over the  $2\pi$  phase range.

All the modulators are driven by a 12 GSa  $s^{-1}$  waveform generator, programmed to encode a 25040-pulse long pseudo-random pattern. For more information on this refer to the Supplementary Materials.

The PMs are followed by an electrically driven polarisation controller (EPC), a variable optical attenuator (VOA), and a 99:1 beam splitter (BS). The EPC is used to control the polarisation of the  $\lambda_1$  photons after transmission through the channel. Each user has a continuous polarisation optimisation routine that aligns the quantum signals to polarise along the preferred optical axis at Charlie.

The VOA sets the flux of the quantum signal before injection into the quantum channel, through a flux calibration control loop that continuously adjusts the VOA so as to have a stable optical output, monitored at the strong output of the BS.

**Feedback systems.** The dual band phase-stabilisation strategy employed in this experiment enabled us to stabilise the quantum channel without affecting the encoding in the wavelength reserved for the quantum signal ( $\lambda_1$ ) or the clock rate of the protocol, which was kept at 500 MHz at all the tested distances. Its general design is presented in Fig. 1 and its detailed block diagram is given in Fig. 5. The top diagram

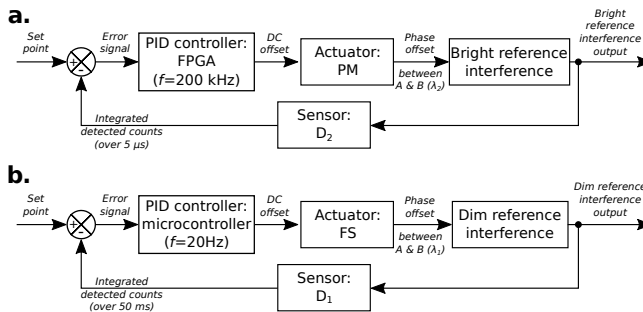


FIG. 5. **Block diagrams of the phase-stabilisation system.** Top: Stage-1 compensation. Bottom: Stage-2 compensation.

shows the stabilisation method based on the bright reference at  $\lambda_2$ . It features a closed loop cycle that locks the interference between Alice’s and Bob’s bright reference beams to

a given intensity level. This, in turn, locks the phase offset between these signals to a fixed value. The bright reference interference is monitored by the SNSPD  $D_2$ . Single photons detected by  $D_2$  are integrated over a period of 5  $\mu$ s. The difference between the integrated number of counts and the set value, constitutes the error signal of a PID controller implemented with an FPGA clocked at 200 kHz. By tuning the DC offset of a phase modulator (PM) that acts on the light coming from Bob, the FPGA controls the interference between the bright references. It is important to notice here that the phase shift applied by the PM affects both the wavelengths  $\lambda_2$  and  $\lambda_1$ . The feedback based on  $\lambda_2$  fully stabilises the bright reference light while it only partially stabilises the quantum one. As explained in the main text, the remaining phase drift of the quantum light is related to the wavelength difference  $\lambda_2 - \lambda_1$ . The reduction factor in phase drift rate for  $\lambda_1$  after stage-1 stabilisation is measured to be  $\sim 16000$ .

The bottom diagram in Fig. 5 refers to the additional stabilisation with the dim reference, which corrects the residual phase drift on  $\lambda_1$ . The error signal for it is provided by the overall interference of quantum signals and dim reference. The quantum signals are interleaved with the dim reference pulses, which are unmodulated and have the same intensity as the brightest decoy pulse ( $u$ ). The presence of dim reference pulses guarantees that the averaged output of the interference is directly related to the residual phase offset in  $\lambda_1$ . This is retrieved by integrating the single photons detected by SNSPD  $D_1$  over 50 ms or 100 ms, depending on the distance. The difference between this value and a set value provides the error signal for a PID controller implemented with a micro-controller operating at the frequency of 20 Hz or 10 Hz, depending on the distance. The micro-controller corrects the phase offset by modulating a fibre stretcher acting on the quantum signal coming from Alice. Differently from the stabilisation in  $\lambda_2$ , the one in  $\lambda_1$  acts solely on the quantum signals and can therefore correct its residual phase drift.

**Protocols.** To demonstrate the multi-protocol aspect of our system, we implemented different variants of TF-QKD, in different regimes. We list them as CAL [22], SNS [24–26] and TWCC-SNS [27]. Their detailed description and security proofs can be found in the referenced papers. See also Methods in [13]. Here we describe our encoding method and the equations used to extract the secret key rate from each protocol.

In all protocols, we consider a symmetric situation, with identical photon fluxes for the users Alice and Bob. This is the real situation in the experiment, where fibre lengths and losses between the users and Charlie are nearly identical (see e.g. Table II in Supplementary Materials). Therefore we only describe the relevant steps for the user Alice; Bob will execute similar operations in his own location. During the preparation stage, Alice generates weak coherent states of the form  $|\sqrt{\mu}e^{i\theta}\rangle$ . She randomly selects a basis  $X$  or  $Z$  with probabilities  $P_X$  or  $P_Z$  ( $P_X + P_Z = 1$ ). If she chooses  $X$  (test basis), she randomly selects a flux value  $\mu = \{u, v, w\}$  with conditional probability  $P_{\mu|X} = \{P_{u|X}, P_{v|X}, P_{w|X}\}$ ,  $P_{u|X} + P_{v|X} + P_{w|X} = 1$ , and a random global phase value  $\phi \in [0, 2\pi]$ . She then prepares and sends the phase-randomised weak coherent state  $|\sqrt{\mu}e^{i\phi}\rangle$ . If she chooses  $Z$  (code basis), she randomly selects a bit value  $\alpha = \{0, 1\}$  and sets the photon flux to  $\mu = \{s, n\}$  with conditional probability  $P_{\mu|Z} = \{P_{s|Z}, P_{n|Z}\}$ ,  $P_{s|Z} + P_{n|Z} = 1$ . In CAL, bits are encoded as coherent states

$|\sqrt{s}e^{i\alpha\pi}\rangle$ . In SNS, bits are encoded on the photon flux, with  $s$  ( $n$ ) representing a bit value 1 (0) for Alice and a bit value 0 (1) for Bob. With our encoder, the photon fluxes  $w$  and  $n$  are both very small, in the order of  $10^{-4}$ . Therefore sending out a photon flux  $n$ , or  $w$ , is equivalent by all practical means to not sending out any flux at all. We denote the probability of ‘not sending’ conditional on choosing the  $Z$  basis as  $P_{n|Z}$  and the probability of sending a photon flux  $s$  conditional on the  $Z$  basis as  $P_{s|Z}$  or simply  $\epsilon$ . The detailed values of the parameters used in the experiment depend on the protocol (CAL, SNS, TWCC) and on the regime (asymptotic or finite-size) adopted. They are listed in Tables III and IV in the supplementary materials.

After the preparation stage, Alice and Bob send their pulses to central node, Charlie. Charlie should interfere the received pulses on a beam splitter and measure the result, announcing publicly which detector click. If Charlie is malicious and adopts a different detection and announcement strategy the security of TF-QKD remains unaffected. After a total of  $N_0$  signals have been sent, the quantum transmission is over and Charlie publicly announces his measurements. When Charlie’s announcement is complete, the users announce their bases. For the  $X$  basis, they also disclose their intensities  $\mu$  and, limitedly to the SNS protocol, they announce the values of their global phases  $\phi$ . Alice and Bob post-select the events for which they used matching bases and intensities. For SNS, they also select the events with global phase values not mismatched by more than  $\Delta$  modulo  $\pi$ . The users extract the bits from the  $Z$  basis events and use the  $X$  basis events to perform the security analysis. In TWCC, the bits in the string distilled from the  $Z$  basis are randomly paired and bit-wise XOR-ed. More specifically, Bob randomly pairs the bits up and announces the positions and parities of each pair. Alice uses this information to repeat this step with her own string and announces the instances for which her parity calculation matches Bob’s one. The users will discard both bits in the pair if the announced parities are different. If the parities are the same, the users keep the first bit of the pairs and form a new shorter string from which they will extract the final key. To this end, they run classical post-processing procedures such as error correction and privacy amplification. The amount of privacy amplification needed to securely distil a key depends on the security analysis and the resulting rate equation. In the following, we list the rate equation adopted for each situation analysed in the experiment.

**CAL PROTOCOL.** This protocol is analysed in the asymptotic scenario for which  $P_Z \approx 1$ . The corresponding SKR equation is the one given for ‘protocol 3’ in [22] and the procedure we use to calculate it is similar to the one described in [13]. See also [16]. The SKR is the sum of two separate contributions, calculated from each detector  $D_0$  and  $D_1$  independently:  $R_{\text{CAL}} = R_{\text{CAL}}^{D_0} + R_{\text{CAL}}^{D_1}$ . We write the contribution from  $D_0$  as

$$R_{\text{CAL}}^{D_0} = Q^z [1 - f_{\text{EC}}h(E^z) - h(\bar{e}_1^{\text{ph}})]. \quad (1)$$

The SKR pertaining to  $D_1$  has a similar expression. In Eq. (1),  $h$  is the binary entropy function,  $f_{\text{EC}}$  is the error correction factor and  $Q^z$  and  $E^z$  are the gain and the bit error rate, respectively, of the protocol, measured in the experiment from the  $D_0$  clicks when the users announce the  $Z$  basis. The quantity  $\bar{e}_1^{\text{ph}}$  is the upper bound to the phase error

rate, for which we have [22]

$$\bar{e}_1^{\text{ph}} = \frac{1}{Q^z} \sum_{j=0,1} \left[ \sum_{m,n=0}^{N_{\text{cut}}} c_m^{(j)} c_n^{(j)} \sqrt{g_{mn}(\bar{Y}_{mn}^x, Y_{\text{cut}})} \right]^2. \quad (2)$$

In Eq. (2), the coefficient  $c_k^{(0)}$  ( $c_k^{(1)}$ ) is defined as  $c_k^{(0)} = e^{-\mu/2} \mu^{k/2} / \sqrt{k!}$  when the integer  $k$  is even (odd) and 0 otherwise;  $g_{mn}(\bar{Y}_{mn}^x, Y_{\text{cut}})$  is a function equal to  $\bar{Y}_{mn}^x$  if  $m+n < Y_{\text{cut}}$  and equal to 1 otherwise;  $Y_{\text{cut}}, N_{\text{cut}}$  are two integers such that  $Y_{\text{cut}} < N_{\text{cut}}$ . In our experiment we set  $Y_{\text{cut}} = 8$  and  $N_{\text{cut}} = 12$ . The quantities  $\bar{Y}_{mn}^x$  are upper bounds for the yields obtained when Alice (Bob) sends  $m$  ( $n$ ) photons. These are estimated using a constrained optimisation linear program [13] similar to the standard decoy state technique [33, 34], with the difference that the yields have to be maximised rather than minimised to provide the worst-case phase error rate. In our implementation, we measured all the intensity combinations  $uu, uv, uw, vv, vw$  and  $ww$  to improve the decoy-state estimation. In parallel to this numerical estimation, we also implemented the analytical estimation given in [16] to verify the correctness of our results.

**SNS PROTOCOL.** The SKR for this protocol in the asymptotic scenario ( $P_Z \approx 1$ ) can be written as [24, 27]

$$R_{\text{SNS}} = \underline{Q}_0 + \underline{Q}_1 [1 - h(\bar{e}_1^{\text{ph}})] - f_{\text{EC}} Q^z h(E^z). \quad (3)$$

In Eq. (3),  $Q^z$  and  $E^z$  are the gain and the bit error rate, respectively, of the protocol, measured in the experiment. The 0-photon gain and 1-photon gain in the  $Z$  basis are  $\underline{Q}_0 = 2\epsilon(1-\epsilon)e^{-s}e^{-n}\underline{y}_0$  and  $\underline{Q}_1 = 2\epsilon(1-\epsilon)(se^{-s}e^{-n} + ne^{-n}e^{-s})\underline{y}_1$ , respectively. The parameters  $\underline{y}_1$  ( $\underline{y}_0$ ) and  $\bar{e}_1^{\text{ph}}$  are, respectively, the lower bound for the single-photon (zero-photon) yield and the upper bound for the single-photon phase error rate. These quantities are drawn from the  $X$  basis of the protocol using equations similar to the ones seen in decoy-states QKD [24, 33, 34].

**TWCC PROTOCOL.** With the addition of two-way classical communication (TWCC), the users can improve the quality of their data before performing the standard error correction and privacy amplification operations. The SKR in the asymptotic scenario for this protocol is [27]

$$R_{\text{TWCC}} = \frac{1}{N_0} \{ \tilde{n}_1 [1 - h(\bar{e}_1^{\text{ph}})] - \text{leak}_{\text{EC}} \}, \quad (4)$$

with  $\tilde{n}_1 = n_1^2 / (2n_t)$ ,  $\bar{e}_1^{\text{ph}} = 2\bar{e}_1^{\text{ph}}(1 - \bar{e}_1^{\text{ph}})$ ,  $\text{leak}_{\text{EC}} = f_{\text{EC}}[n_a h(E_a) + n_b h(E_b) + n_c h(E_c)]$ . Here,  $n_1 = N_0 \underline{Q}_1$  is the number of untagged bits and  $n_t = N_0 Q^z$  is the number of successful detections, an observable of the protocol, with  $N_0$  the total number of prepared states. The term ‘leak<sub>EC</sub>’ represents the number of bits to be exchanged during the error correction procedure. The quantities  $n_a$  and  $E_a$  are the number of bits and the error rate, respectively, in Bob’s string associated with an odd parity when paired during the TWCC procedure. Similarly, the quantities  $n_b$  and  $E_b$  ( $n_c$  and  $E_c$ ) are the number of bits and the error rate, respectively, in Bob’s string associated with an even parity and when both bits are 0 (1), when paired during the TWCC procedure. The other quantities are as in Eq. (3).

**FINITE-SIZE SNS AND TWCC.** The finite size analysis of TWCC [18] is derived directly from the one of SNS [25, 26]. The error correction term of the asymptotic rate equation (4)

remains unchanged but the remaining terms are modified to take into account the leakage of information due to finite-size statistical effects. The number of secret bits in the finite-size regime after TWCC has been performed is given by

$$n_{\text{TWCC-FS}} = \hat{n}_1[1 - h(\hat{e}_1^{\text{ph}})] - \text{leak}_{\text{EC}} - \Delta, \quad (5)$$

with  $\Delta = \log_2(2/\epsilon_{\text{EC}}) - 2 \log_2(\sqrt{2}\epsilon_{\text{PA}}\hat{\epsilon})$  the finite-size correction term and with  $\epsilon_{\text{EC}}$ ,  $\epsilon_{\text{PA}}$  and  $\hat{\epsilon}$  the failure probabilities for error correction, privacy amplification and the choice of the smoothing parameter, respectively. With the right choice of parameters, our implementation features a security parameter of  $2.2 \times 10^{-9}$ , which is the same as in [18]. The hatted quantities  $\hat{n}_1$  and  $\hat{e}_1^{\text{ph}}$  correspond to the tilded quantities in Eq. (4), but calculated in the finite-size regime using a composable definition of security and the Chernoff bound. Their detailed expressions can be found in the reference paper [25].

**Binary maps generation.** From experiments of the SNS TF-QKD protocol described, real keys were extracted. To achieve this, single time-tagged events, acquired in 500 ps windows, were processed individually. Sifting Charlie's announcements, clicks in the  $Z$  basis from both detectors were isolated and concatenated. They were then used by Alice and Bob to separately generate their own initial key string. For every photon click recorded in  $Z$  basis, Alice (Bob) registers a bit 1 (0) if she (he) had sent a weak-coherent pulse within the time slot and a bit 0 (1) if she (he) had chosen not to send anything. As a result, they obtain matching bits in the cases where only one user has prepared and sent a pulse and opposite bits if both sent. The latter, accompanied by dark counts, contributes to the QBER in the key generation basis. A sample of these initial keys for Alice and Bob are shown in the first two squares of Fig. 4, in the form of binary maps comprised of 128x128 pixels, for the finite-size measurement taken at 522 km. Zeroes and ones are represented by white and black pixels respectively. The white-bias of Alice and black bias of Bob are expected and attributed to the send-send clicks that have the highest occurrence probability and in which Alice will always obtain a 1 while Bob will obtain a 0.

Initial keys were post-processed according to the two-way classical communication method to reduce their initial QBER of 16% and allow successful QKD at such long distances. During this process, Bob's bits are randomly paired up and their parity calculated. The pair positions and resulting parity must be publicly announced so that the procedure can be repeated by Alice who will also announce her results. The initial keys are then further sifted to include only the first bit of pairs whose parity matched in both users. For instance, given the SNS encoding in the key generation basis, pairs encoded as 'sn' by Alice (see Protocols in Methods) in a randomly selected pair will provide a matching parity if paired with bits encoded as 'ns' by Bob whereas will provide unmatched parity if paired with bits encoded as 'ss' by Bob. Although TWCC reduces the length of the secret key, it also significantly reduces the QBER so that the overall signal to noise ratio is increased. The effect of the process on the 522 km data is shown in the first two rectangles at the bottom of Fig. 4. The binary map is reduced in dimension by 70% to represent the equivalent reduction in the entire bit strings. The white, black bias is also visibly reduced. To better depict the QBER reduction the binary maps are bitwise XORed before and after TWCC in the rightmost boxes of Fig. 4. Matching and

opposite bits are represented by white and black pixels respectively. In this case, the QBER is reduced by over a factor 4.5, from 16% to 3.5%, thus allowing us to extract a secret key at distances up to 604.8 km.

---

**SUPPLEMENTARY INFORMATION FOR  
600 KM REPEATER-LIKE QUANTUM COMMUNICATIONS WITH DUAL-BAND STABILISATION**

Mirko Pittaluga<sup>1,2†\*</sup>, Mariella Minder<sup>1,3†</sup>, Marco Lucamarini<sup>1\*</sup>, Mirko Sanzaro<sup>1</sup>, Robert I. Woodward<sup>1</sup>, Ming-Jun Li<sup>4</sup>, Zhiliang Yuan<sup>1</sup> & Anderw J. Shields<sup>1</sup>

<sup>1</sup>*Toshiba Europe Limited, 208 Cambridge Science Park, Cambridge CB4 0GZ, UK*

<sup>2</sup>*School of Electronic and Electrical Engineering, University of Leeds, Leeds LS2 9JT, UK*

<sup>3</sup>*Department of Engineering, Cambridge University, 9JJ Thomson Avenue, Cambridge CB3 0FA, UK*

<sup>4</sup>*Corning Incorporated, Corning, New York, 14831, USA*

†*These authors contributed equally to this work*

\**mirko.pittaluga@crl.toshiba.co.uk*

\**email: marco.lucamarini@crl.toshiba.co.uk*

### SYSTEM CHARACTERISATION

In Tab. I is reported a detailed characterisation of the experimental setup. This table highlights an asymmetry between the users' insertion losses at Charlie. The asymmetry is related to the two different types of modulators acting on the incoming signals. A phase modulator is lossier than a fibre stretcher (which is almost lossless), and therefore Charlie's system transmission for Bob is lower than for Alice. In the protocol simulations, we used the lowest transmission figure to characterise the losses at the receiver. We exploited Alice's higher transmission coefficient to compensate for a small asymmetry in the quantum channels losses.

In Tab. I we present two different dark counts figures. The first is derived from the SNSPDs (Single Quantum EOS 410 CS cooled at 2.9 K) characterisation, executed with no connected fibre. The second is extracted from the experimental data during protocol execution. We associate the increase in dark counts in the second case to environmental contaminations and to the scattering occurring in the fibres. This figure could be further reduced by using narrower spectral filters.

Charlie's system transmission (from Alice)	62.86%
Charlie's system transmission (from Bob)	50.77%
Efficiency SNSPD D <sub>0</sub>	73%
Efficiency SNSPD D <sub>1</sub>	77%
SNSPD dark counts (calibration)	10 Hz
SNSPD dark counts (experiment)	14 Hz
Clock rate for quantum signal	500 MHz

TABLE I. Experimental parameters of the setup.

In Tab. II we report the combined losses of the fibre spools used at the different distances. At all distances, we have assigned the lossier spools to Bob. During the experiment, when there was an asymmetry between the users' photon rate received by Charlie, we compensated for it by increasing the attenuation of Bob's transmitter.

Fibre length	Losses (dB)	
	Alice	Bob
76.641 km	13.30	13.25
184.351 km	32.20	31.39
260.866 km	45.39	44.70
277.461 km	48.46	47.73
302.585 km	53.13	52.38

TABLE II. Combined losses of the fibre spools used at different distances.

### ENCODING PARAMETERS

In this experiment we tested different TF-QKD protocols: a phase matching version [22], and the SNS version [24]. The latter, with and without TWCC ([25, 27]). For all the measurements we used a 25040 pulses long pattern. Half of the pulses were used for the protocol encoding (dim quantum). Interleaved to these, phase unmodulated pulses were used as quantum references (dim reference). The pattern encoding was executed by two time-synchronised pattern generators, which controlled the phase and intensity modulators described in the Methods. For every protocol, the pattern properties have been chosen with the aim of maximising the communication distance. With the exception of the point at 604.8 km, the two versions of the TWCC SNS protocol (asymptotic and finite size) used the same pattern over the different tested distances.

The way we encode the patterns is by fair sampling. Using the pattern properties shown in Tab. III and IV, for each protocol we calculate the probabilities of the different users' pulses combinations. At this point, we generate a 12520-elements-long list of pulses pairs reflecting the matching probabilities. This list is then randomly shuffled, resulting in two patterns with a random pulse distribution that respects the matching probabilities expected by the protocol simulations.

Tab. III summarises the photon fluxes and the pattern probabilities used for the CAL TF-QKD protocol. In this protocol the *X* basis is the one used for coding, while the *Z* is used for testing (decoy states). Pulses in the *X* basis can only take two phase values: either  $+\pi/2$  or  $-\pi/2$ . Their intensity is set to be equal to the one of

the  $v$  decoy pulses. Pulses in the  $Z$  basis on the contrary are all phase randomised. Since this protocol has been run only in the asymptotic regime, for the purpose of the key rate estimation, calculations have been carried out by normalising  $P_X$  from the original 50% to 99.9%.

Fibre length (km)	CAL asympt.
	368.7
$s$ (ph/pulse)	0.015
$u$ (ph/pulse)	0.1
$v$ (ph/pulse)	0.015
$w$ (ph/pulse)	0.0002
$P_Z$ (code basis)	50.0%
$P_X$ (test basis)	50.0%
$P_u$	33.3%
$P_v$	33.3%
$P_w$	33.3%
Secret key rate	852.7 bps

TABLE III. Secret key rate and parameters used for the implementation of the CAL TF-QKD protocol [22] in the asymptotic scenario.  $s$  is the photon flux used for signal pulses, while  $u, v, w$  are the photon fluxes used for the decoy states.  $P_Z$  is the users' probability of sending a pulse in the code basis.  $P_X$  is the users' probability of sending a pulse in the test basis,  $P_u, P_v, P_w$  are the probabilities of sending the  $u, v, w$  decoy pulses respectively.

Tab. IV summarises the parameters for the different configurations of the SNS TF-QKD protocol we tested. In the SNS protocol, the  $Z$  basis is the one used for the

key generation (sending-or-not-sending), while the  $X$  basis is used for testing the quantum channel (decoy states). In this protocol, all the encoded pulses (dim quantum) are phase randomised. Also for SNS, in the asymptotic case the key rate estimation was executed by normalising the probability of using the coding basis  $P_Z$  from 50% to 99.9%.

Fibre length (km)	SNS asympt.	TWCC SNS asympt.	SNS finite size	
	368.7	all except 605	605	all
$s$ (ph/pulse)	0.35	0.35	0.38	0.4
$u$ (ph/pulse)	0.35	0.35	0.38	0.4
$v$ (ph/pulse)	0.035	0.0105	0.01065	0.075
$w$ (ph/pulse)	0.0002	0.0002	0.00023	0.0002
$P_Z$ (code basis)	50.0%	50.0%	50.0%	60.0%
$P_s$	5.8%	13.0%	7.5%	
$P_X$ (test basis)	50.0%	50.0%	50.0%	40.0%
$P_u$	33.3%	33.3%	33.3%	20.0%
$P_v$	33.3%	33.3%	33.3%	60.0%
$P_w$	33.3%	33.3%	33.3%	20.0%

TABLE IV. Parameters of the patterns used for the implementation of the SNS TF-QKD protocol [24] in different experimental scenarios (with or without TWCC [25, 27], in the asymptotic or finite-size regimes).  $s$  is the photon flux used for signal pulses, while  $u, v, w$  are the photon fluxes used for the decoy states.  $P_Z$  is the users' probability of choosing to encode a pulse in the code basis,  $P_s$  is the probability of actually sending a signal when the  $Z$  basis is chosen.  $P_X$  is the users' probability of encoding a pulse in the test basis,  $P_u, P_v, P_w$  are the probabilities of sending the  $u, v, w$  decoy pulses respectively.

## EXPERIMENTAL RESULTS FOR SNS-TYPE PROTOCOLS

In Tab. V, VI and VII we report the detailed experimental results for the different SNS-type protocols tested. Tab. V is reporting the results for the asymptotic SNS protocol (without TWCC). Tab. VI summarises the results for the TWCC SNS TF-QKD protocol in the asymptotic scenario, while the ones in the finite size regime are reported in Tab. VI. In all the tables are reported the distances at which the experiments were executed and the number of protocol encoded pulses that were sent ( $N_0$ ). Also reported are the errors in the different bases and for different pulses intensities, and the calculated secret key rate (SRK) obtained at that distance (alongside the relative  $SKC_0$  bound). For all the protocols, the exact number of pulses sent in each pulses pair configuration can be calculated by multiplying the respective configuration probabilities (deducible from Tab. III and IV) by  $N_0$ . The number of pulses detected in these configurations are reported in the tables below, labelled in the format  $B_1B_2t_1t_2$ , where  $B_1$  and  $t_1$  ( $B_2$  and  $t_2$ ) are the basis and the type of pulse sent by Alice (Bob). When TWCC is employed, quantities relative to the key post-processing are listed.

Fibre Length (km)	368.702
$N_0$	$2.066 \cdot 10^{11}$
Phase mismatch acceptance	$22.5^\circ$
Z error rate	6.59%
Xuu error rate	3.29%
Xvv error rate	3.87%
Phase error rate	4.15%
SKR SNS (no TWCC) asympt norm (bit/signal)	$1.098 \cdot 10^{-6}$
SKR SNS (no TWCC) asympt norm (bit/s)	$5.492 \cdot 10^2$
Ratio SKR over SKC <sub>0</sub>	1.54
SKC <sub>0</sub> (bit/signal)	$7.151 \cdot 10^{-7}$
SKC <sub>0</sub> (bit/s)	$3.576 \cdot 10^2$
Total Detected $D_0$	4624363
Total Detected $D_1$	4887891
Detected ZZss	39403
Detected ZZsn	314309
Detected ZZns	304872
Detected ZZnn	4264
Detected ZXsu	217790
Detected ZXsv	121824
Detected ZXsw	112334
Detected ZXnu	1729304
Detected ZXnv	173107
Detected ZXnw	1634
Detected XZus	217780
Detected XZun	1786996
Detected XZvs	117638
Detected XZvn	155240
Detected XZws	113964
Detected XZwn	1486
Detected XXuu	1240351
Detected XXuv	685682
Detected XXuw	643480
Detected XXvu	668424
Detected XXvv	115296
Detected XXvw	55695
Detected XXwu	628786
Detected XXvv	62043
Detected XXww	552
Detected XXuu matching ( $D_0$ )	74844
Detected XXuu matching ( $D_1$ )	79037
Correct XXuu matching ( $D_0$ )	72352
Correct XXuu matching ( $D_1$ )	76474
Detected ZZ errors	43667
Detected ZZ correct	619181

TABLE V. Asymptotic SNS: experimental results for a fibre length of 368.7 km.

Fibre Length (km)	153.282	368.702	521.982	555.172	605.17
$N_0$	$5.296 \cdot 10^{10}$	$1.527 \cdot 10^{11}$	$5.208 \cdot 10^{11}$	$2.554 \cdot 10^{11}$	$1.002 \cdot 10^{12}$
Phase mismatch acceptance	22.5°	22.5°	22.5°	22.5°	22.5°
Z error rate (before)	13.1%	13.1%	14.%	14.6%	16.4%
Odd pairs in raw keys	$3.522 \cdot 10^6$	$2.277 \cdot 10^5$	$3.968 \cdot 10^4$	$9.565 \cdot 10^3$	$1.369 \cdot 10^4$
Even pairs 00 in raw keys	$1.938 \cdot 10^6$	$1.228 \cdot 10^5$	$2.162 \cdot 10^4$	$5.174 \cdot 10^3$	$7.411 \cdot 10^3$
Even pairs 11 in raw keys	$1.74 \cdot 10^6$	$1.15 \cdot 10^5$	$1.963 \cdot 10^4$	$4.725 \cdot 10^3$	$6.575 \cdot 10^3$
Error pairs in raw keys	$1.591 \cdot 10^5$	$1.039 \cdot 10^4$	$2.096 \cdot 10^3$	$5.532 \cdot 10^2$	$1.029 \cdot 10^3$
Z error rate (after)	2.21%	2.23%	2.59%	2.84%	3.72%
Xuu error rate	2.8%	3.21%	3.86%	3.68%	3.5%
Xvv error rate	5.53%	6.32%	4.78%	8.33%	13.6%
Phase error rate	5.68%	6.4%	3.71%	6.08%	2.31%
$n_1$ (before TWCC)	$1.159 \cdot 10^7$	$7.49 \cdot 10^5$	$1.254 \cdot 10^5$	$3.284 \cdot 10^4$	$3.733 \cdot 10^4$
$n_1$ (after TWCC)	$3.605 \cdot 10^6$	$2.326 \cdot 10^5$	$3.685 \cdot 10^4$	$1.04 \cdot 10^4$	$9.136 \cdot 10^3$
$e_1^{\text{ph}}$ (before TWCC)	5.68%	6.4%	3.71%	6.08%	2.31%
$e_1^{\text{ph}}$ (after TWCC - asympt)	10.7%	12.%	7.15%	11.4%	4.52%
SKR TWCC asympt norm (bit/signal)	$7.441 \cdot 10^{-5}$	$1.412 \cdot 10^{-6}$	$8.557 \cdot 10^{-8}$	$2.838 \cdot 10^{-8}$	$1.937 \cdot 10^{-9}$
SKR TWCC asympt norm (bit/s)	$3.721 \cdot 10^4$	$7.059 \cdot 10^2$	$4.278 \cdot 10^1$	$1.419 \cdot 10^1$	$9.685 \cdot 10^{-1}$
Ratio SKR over SKC <sub>0</sub>	0.0215	1.97	50.	61.3	29.7
SKC <sub>0</sub> (bit/signal)	$3.456 \cdot 10^{-3}$	$7.151 \cdot 10^{-7}$	$1.711 \cdot 10^{-9}$	$4.632 \cdot 10^{-10}$	$6.511 \cdot 10^{-11}$
SKC <sub>0</sub> (bit/s)	$1.728 \cdot 10^6$	$3.576 \cdot 10^2$	$8.556 \cdot 10^{-1}$	$2.316 \cdot 10^{-1}$	$3.256 \cdot 10^{-2}$
Total Detected $D_0$	66051719	4241991	745698	181085	263766
Total Detected $D_1$	69221704	4524664	795437	193156	278746
Detected ZZss	2423210	156953	27876	6727	9620
Detected ZZsn	8146041	521082	91891	22168	32219
Detected ZZns	8052039	526583	91497	22122	31538
Detected ZZnn	11389	1380	2024	848	2907
Detected ZXsu	6196623	403188	70879	17076	24785
Detected ZXsv	3217021	205870	36367	8629	12876
Detected ZXsw	3107274	198690	35299	8610	12320
Detected ZXnu	20581340	1349062	235655	57121	81690
Detected ZXnv	604012	37884	7635	1915	3125
Detected ZXnw	4212	518	747	289	1085
Detected XZus	6202770	403207	70119	17168	24722
Detected XZun	20928197	1340008	236339	57217	82636
Detected XZvs	3181382	208453	36111	8811	12607
Detected XZvn	628269	41662	7104	1879	3037
Detected XZws	3078177	202140	35286	8426	12396
Detected XZwn	4250	534	765	281	1102
Detected XXuu	15759404	1022280	179333	43000	61766
Detected XXuv	8202418	526279	92761	22151	32573
Detected XXuw	7977865	511560	89706	21900	31585
Detected XXvu	8127297	531576	92456	22577	31672
Detected XXvv	480868	30579	5527	1427	1904
Detected XXvw	247965	16325	2809	799	1182
Detected XXwu	7874039	516027	89699	22269	31572
Detected XXwv	235716	14614	2968	718	1170
Detected XXww	1645	201	282	113	423
Detected XXuu matching ( $D_0$ )	930327	59658	10558	2581	3712
Detected XXuu matching ( $D_1$ )	990284	64565	11389	2746	3939
Correct XXuu matching ( $D_0$ )	905683	57844	10179	2478	3594
Correct XXuu matching ( $D_1$ )	961135	62388	10921	2653	3789
Detected ZZ errors	2434599	158333	29900	7575	12527
Detected ZZ correct	16198080	1047665	183388	44290	63757

TABLE VI. Asymptotic TWCC SNS: experimental results obtained at various fibre lengths.

Fibre Length (km)	153.282	368.702	521.982	555.172
$N_0$	$6 \cdot 10^{11}$	$2.435 \cdot 10^{12}$	$3.07 \cdot 10^{12}$	$3.536 \cdot 10^{12}$
Phase mismatch acceptance	22.5°	22.5°	22.5°	22.5°
Z error rate (before)	7.67%	7.69%	9.01%	9.77%
Odd pairs in raw keys	$4.164 \cdot 10^7$	$3.564 \cdot 10^6$	$2.333 \cdot 10^5$	$1.336 \cdot 10^5$
Even pairs 00 in raw keys	$2.135 \cdot 10^7$	$1.838 \cdot 10^6$	$1.198 \cdot 10^5$	$6.922 \cdot 10^4$
Even pairs 11 in raw keys	$2.077 \cdot 10^7$	$1.768 \cdot 10^6$	$1.152 \cdot 10^5$	$6.501 \cdot 10^4$
Error pairs in raw keys	$5.738 \cdot 10^5$	$4.938 \cdot 10^4$	$4.542 \cdot 10^3$	$3.103 \cdot 10^3$
Z error rate (after)	0.685%	0.689%	0.97%	1.16%
Xuu error rate	2.69%	2.88%	2.87%	3.47%
Xvv error rate	3.56%	3.81%	5.31%	5.09%
Phase error rate	4.16%	4.47%	6.04%	5.59%
$n_1$ (before TWCC)	$1.185 \cdot 10^8$	$1.003 \cdot 10^7$	$6.4 \cdot 10^5$	$3.652 \cdot 10^5$
$n_1$ (after TWCC)	$3.596 \cdot 10^7$	$3.013 \cdot 10^6$	$1.828 \cdot 10^5$	$1.026 \cdot 10^5$
$e_1^{\text{ph}}$ (before TWCC)	4.23%	4.71%	7.48%	7.65%
$e_1^{\text{ph}}$ (after TWCC)	8.09%	8.98%	13.8%	14.1%
Number of secure bits generated (bits)	$1.707 \cdot 10^7$	$1.329 \cdot 10^6$	$4.046 \cdot 10^4$	$1.745 \cdot 10^4$
SKR (bit/signal)	$2.846 \cdot 10^{-5}$	$5.459 \cdot 10^{-7}$	$1.318 \cdot 10^{-8}$	$4.937 \cdot 10^{-9}$
SKR (bit/s)	$1.423 \cdot 10^4$	$2.729 \cdot 10^2$	6.59	2.468
Ratio SKR over SKC <sub>0</sub>	0.00823	0.763	7.7	10.7
SKC <sub>0</sub> (bit/signal)	$3.456 \cdot 10^{-3}$	$7.151 \cdot 10^{-7}$	$1.711 \cdot 10^{-9}$	$4.632 \cdot 10^{-10}$
SKC <sub>0</sub> (bit/s)	$1.728 \cdot 10^6$	$3.576 \cdot 10^2$	$8.556 \cdot 10^{-1}$	$2.316 \cdot 10^{-1}$
Total Detected $D_0$	601407532	50532067	3317070	1945930
Total Detected $D_1$	623261177	54266217	3616047	2071809
Detected ZZss	14322977	1229675	80689	46061
Detected ZZsn	90153430	7739935	511622	296484
Detected ZZns	90035335	7685653	507468	290238
Detected ZZnn	642059	54944	20176	17462
Detected ZXsu	25714805	2199489	144929	82891
Detected ZXsv	46330397	3956642	262219	150458
Detected ZXsw	12870272	1107377	72977	42765
Detected ZXnu	159718589	13637478	898693	517464
Detected ZXnv	90956994	7710475	507227	297300
Detected ZXnw	93804	7989	2973	2550
Detected XZus	25704406	2209257	146032	85067
Detected XZun	159575781	13695784	906734	526484
Detected XZvs	46091214	3944702	259209	149050
Detected XZvn	89990485	7718247	507676	294097
Detected XZws	12982067	1109205	73179	42204
Detected XZwn	92445	7776	2977	2516
Detected XXuu	44724005	3838050	252841	145782
Detected XXuv	82278922	7047247	466076	270776
Detected XXuw	22992576	1978960	131444	75985
Detected XXvu	82116355	7042214	463506	268561
Detected XXvv	78177798	6684280	437657	252988
Detected XXvw	13010771	1116305	73487	42281
Detected XXwu	22952199	1964545	129678	75082
Detected XXwv	13127709	1110997	73238	42795
Detected XXww	13314	1058	410	398
Detected XXuu matching ( $D_0$ )	2822546	239368	15656	9148
Detected XXuu matching ( $D_1$ )	2880087	250202	16753	9609
Correct XXuu matching ( $D_0$ )	2743311	232285	15215	8846
Correct XXuu matching ( $D_1$ )	2805790	243186	16263	9260
Detected ZZ errors	14965036	1284619	100865	63523
Detected ZZ correct	180188765	15425588	1019090	586722

TABLE VII. Finite-size TWCC SNS: experimental results obtained at various fibre lengths.